MAGNETIC RESONANCE

CrossMark

Intra-individual comparison of gadolinium-enhanced MRI using pseudo-golden-angle radial acquisition with gadoxetic acid-enhanced MRI for diagnosis of HCCs using LI-RADS

Yoon-Chul Kim[1] · Ji Hye Min[2] · Young Kon Kim[3] · Soon Jin Lee[3] · Soohyun Ahn[4] · Eunju Kim[5] · Hans Peeters[6]

Abstract

Objectives To determine the usefulness of extracellular contrast agent (ECA)-enhanced multiphasic liver magnetic resonance imaging (MRI) using a pseudo-golden-angle radial acquisition scheme by intra-individual comparison with gadoxetic acid-MRI (EOB-MRI) with regard to image quality and the diagnosis of hepatocellular carcinoma (HCC).

Materials and methods This prospective study enrolled 15 patients with 18 HCCs who underwent EOB-MRI using a Cartesian approach and ECA-MRI using the pseudo-golden-angle radial acquisition scheme (free-breathing continuous data acquisition for 64 s following ECA injection, generating six images). Two reviewers evaluated the arterial and portal phases of each MRI for artifacts, organ sharpness, and conspicuity of intrahepatic vessels and the hepatic tumors. A Liver Imaging Reporting and Data System category was also assigned to each lesion.

Results There were no differences in the subjective image quality analysis between the arterial phases of two MRIs ($p > 0.05$). However, ghosting artifact was seen only in EOB-MRI ($N = 3$). Six HCCs showed different signal intensities in the arterial phase or portal phase between the two MRIs; five HCCs showed arterial hyperenhancement on ECA-MRI, but not on EOB-MRI. The capsule was observed in 15 HCCs on ECA-MRI and 6 HCCs on EOB-MRI. Five and one HCC were assigned as LR-5 and LR-4 with ECA-MRI and LR-4 and LR-3 with EOB-MRI, respectively.

Conclusion Free-breathing ECA-enhanced multiphasic liver MRI using a pseudo-golden-angle radial acquisition was more sensitive in detecting arterial hyperenhancement of HCC than conventional EOB-MRI, and the image quality was acceptable.

Key Points
• *The pseudo-golden-angle radial acquisition scheme can be applied to perform free-breathing multiphasic dynamic liver MRI.*
• *Adopting the pseudo-golden-angle radial acquisition scheme can improve the detection of arterial enhancement of HCC.*
• *The pseudo-golden-angle radial acquisition scheme enables motion-free liver MRI.*

Keywords Magnetic resonance imaging · Carcinoma · Hepatocellular · Liver · Artifacts

✉ Young Kon Kim
  kimjmyr0707@naver.com; youngkon0707.kim@samsung.com

1   Clinical Research Institute, Samsung Medical Center, Sungkyunkwan University School of Medicine, Seoul, Republic of Korea

2   Department of Radiology, Chungnam National University Hospital, Chungnam National University College of Medicine, 282 Munhwa-ro, Jung-gu, Daejeon 35015, Republic of Korea

3   Department of Radiology and Center for Imaging Science, Samsung Medical Center, Sungkyunkwan University School of Medicine, 81 Ilwon-Ro, Gangnam-gu, Seoul 06351, Republic of Korea

4   Department of Mathematics, Ajou University, Suwon, Republic of Korea

5   MR Clinical Scientist Philips Korea, Sowol-ro 2-gil, Joong-gu, Seoul, Republic of Korea

6   MR Clinical Scientist Philips Netherlands: Veenpluis 4-6, Building QR-0.113, 5684 PC , Best, Netherlands

Abbreviations

AP	Arterial phase
ECA	Extracellular contrast agent
EOB-MRI	Gadoxetic acid-enhanced MRI
GRASP	Golden-angle radial sparse parallel
HBP	Hepatobiliary phase
HCC	Hepatocellular carcinoma
LI-RADS	Liver Imaging Reporting and Data System
MRI	Magnetic resonance imaging
PGRA	Pseudo-golden-angle radial acquisition scheme
PVP	Portal venous phase

Introduction

Based on the substantial advances in image quality over the past decade, it is generally accepted that contrast-enhanced dynamic liver magnetic resonance imaging (MRI) outperforms computed tomography in the diagnosis of hepatocellular carcinoma (HCC) [1–3]. Initially, the HCC diagnostic criteria was based on extracellular contrast agent (ECA)-enhanced imaging [4]. But then gadoxetic acid (Gd-EOB-DTPA, Primovist [Eovist in the USA], Bayer) opened a new horizon for HCC diagnosis as it offers high sensitivity for HCC detection by providing with hepatobiliary phase (HBP) [5, 6]. However, several limitations in liver MRI remained unsolved: one the most important issue is the long scan time required for imaging that often cannot be achieved within a single breath-hold, now and then causing respiratory motion artifacts. This served as a major reason for poor image quality especially for dynamic contrast-enhanced sequences.

Recently, Akai et al reported that gadoxetic acid increased the respiratory rate rapidly, and the effect on respiration tended to be larger than gadoteridol and gadopentetate dimeglumine [7]. The ghosting artifacts during the arterial phase (AP) of gadoxetic acid-enhanced MRI (EOB-MRI) is reported to range from 4.8 to 19%, leading to suboptimal or nondiagnostic imaging [8–10]. Several strategies have been proposed to overcome such artifacts, including shortened scanning time [8, 11], lowered contrast injection rate [12, 13], contrast dilution using saline [14], modified breath-holding or extended breathing method [15, 16], and radial acquisition technique [17]. This is an important issue because the AP is essential for detecting HCC [18]. In addition, since gadoxetic acid is formulated in half the volume (0.1 mL/kg) containing a quarter of the concentration of gadolinium, it is difficult to catch the arterial bolus during the optimum late arterial phase for HCC detection [19].

Multiple APs could increase the probability of capturing the optimal instance of arterial hyperenhancement of HCC [20]. In terms of artifacts, multiple APs might be beneficial for minimizing the ghosting artifact during the AP of EOB-MRI [8]. As a more innovative approach, a recently introduced novel method, known as GRASP (golden-angle radial sparse parallel), for rapid acquisition of data using compressed sensing [21], parallel imaging, and a golden-angle acquisition scheme could potentially overcome the aforementioned limitations in AP imaging [22–25]. This approach employs a non-Cartesian "stack-of-stars" trajectory to acquire volumetric k-space data. The radial sampling is performed using the golden-angle radial sampling scheme, where the angle of the radial lines is increased continuously by 111.25°, by which a rather uniform coverage of k-space with high temporal incoherence is obtained for any arbitrary number of consecutive lines [26, 27]. This enables dynamic MRI using continuous data acquisition and retrospective reconstruction of an image series with arbitrary temporal resolution by grouping different numbers of consecutive radial lines into temporal frames [28, 29]. The pseudo-golden-angle radial acquisition scheme (PGRA), similar to GRASP, employs a more flexible angle between consecutive lines rather than 111.25°, to provide evenly distributed k-space radial lines for any arbitrary number of projections and in turn reduces streaky artifact and scan time [30].

A few studies have applied GRASP to liver MRI [23–26, 31]. However, no study has applied a golden-angle acquisition scheme to liver MRI with regard to HCC evaluation. The goal of this prospective study was to determine the feasibility of ECA-enhanced multiphasic liver MRI using PGRA comparing it with EOB-MRI using a conventional Cartesian approach in terms of image quality and the diagnostic performance of HCC.

Materials and methods

Patients

This prospective study was approved by our institutional review board and followed the Declaration of Helsinki and subsequent amendments. Written informed consent was obtained from each patient before enrollment in the study. Between November 2017 and February 2018, we recruited adults (≥ 18 years old) with chronic hepatitis or cirrhosis who had been referred to Samsung Medical Center, Seoul, Korea, an academic referral institution, due to a suspected hepatic tumor on ultrasound. The inclusion criteria for this crossover intra-individual comparison of the two MRIs were (a) patients with a first-time diagnosis of a hepatic nodule on an initial MRI and (b) patients who were scheduled to undergo liver surgery. Since our institutional policy prefers EOB-MRI over ECA-MRI for patients suspected of having HCC, most patients had undergone EOB-MRI as the first MR examination, followed by ECA-MRI. We excluded patients who had refused consent ($N = 5$), and those who had a longer than 1-month time interval between the two MR examinations ($N = 6$). We finally enrolled 15 patients (14 men, 1 woman; age range, 41–69 years; mean, 57.9 years). The two MR

examinations were performed within a 1-month interval (median, 15 days; range, 10 to 22 days). Reference standards for the diagnosis of HCCs were based on histopathological examination of surgical specimens.

MR examination

MRI was acquired using a 3.0-T MR system (Intera Achieva 3.0-T, Philips Healthcare) equipped with 32-channel phased-array receiver coil. Baseline images included a T1-weighted turbo field-echo in-phase and opposed sequence, with breath-hold multishot T2-weighted imaging and respiratory-triggered heavily T2-weighted imaging. Diffusion weighted imaging was acquired using respiratory-triggered single-shot echo planar imaging with a b value of 0, 100, and 800 s/mm^2. For EOB-MRI, unenhanced, AP (25–30 s), portal venous phase (PVP; 60 s), 3-min transitional phase, and 20-min HBP images were obtained using a T1-weighted 3D turbo field-echo sequence (T1 high-resolution isotropic volume examination, THRIVE, Philips Healthcare; TR/TE, 3.1/1.5 ms; flip angle, 10°; matrix size, 256 × 256; bandwidth, 995.7 Hz/pixel). The measured voxel size was $1.5 \times 1.5 \times 4.0$ mm, and the reconstructed voxel size was $1.17 \times 1.17 \times 2.0$ mm. Gadoxetic acid was administered intravenously using a power injector at a rate of 1 mL/s for a dose of 0.025 mmol/kg body weight. The time for AP imaging was determined using the MR fluoroscopic bolus detection technique.

For ECA-MRI, a stack-of-stars three-dimensional (3D) radial GRE sequence with the pseudo-golden-angle ordering scheme (Fig. 1) was used during free-breathing, which was initiated at the time of contrast injection. Gadoterate meglumine (Gd-DOTA, Dotarem®, Guerbet) was administered intravenously using a power injector at a rate of 2 mL/s for a dose of 0.1 mmol/kg body weight, followed by a 20-mL saline flush. No timing run or bolus tracking was performed. A total of 379 radial spokes were continuously acquired in 64 s with the following parameters: slice thickness, 4 mm; flip angle, 10°; field of view, 375 × 375 × 200 mm^3; matrix size, 252 × 252 × 50; spatial resolution, $1.5 \times 1.5 \times 4.0$ mm^3; repetition time/first echo time/s echo time, 3.9 milliseconds (ms)/1.22 ms/2.1 ms; and bandwidth, 1929 Hz/pixel. Fifty partitions were acquired (interpolated) with 0.75 partial-Fourier performed along the slice-encoding dimension. After completion of PGRA, second PVP and 3 min delayed phase were also obtained using a conventional Cartesian approach.

PGRA reconstruction

Raw data was exported after the PGRA scan was terminated. Image reconstruction was performed off-line using the Berkeley Advanced Reconstruction Toolbox (BART) [32] in MATLAB (MathWorks) on a Windows OS with AMD eight-core CPU at 3.6 GHz and 16 GB RAM. The dual echo stack-of-stars 3D golden-angle radial raw data was first sorted into six-dimensional space, in which the dimensions are indicated by (kr, kθ, kz, coil, phase, echo). The number of radial spokes selected determined the number of phases. The reconstructions with different radial spokes of 40, 55, and 70 were performed, and the reconstruction with 55 radial spokes provided a good compromise between temporal fidelity and image SNR. As such, we chose 55 consecutive radial spokes to

Fig. 1 Schema of the sampling scheme for golden-angle radial acquisitions and pseudo-golden-angle radial acquisitions. In golden-angle radial acquisitions, the angle of the acquired spoke is continuously increased by 111.25°, leading to non-equidistantly spaced radial spokes, whereas pseudo-golden-angle radial acquisitions employ more flexible degrees of angle to generate uniform distribution of an arbitrarily determined number of radial spokes. This enables dynamic imaging using continuous data acquisition and retrospective reconstruction of image series with arbitrary temporal resolution by grouping different numbers of consecutive spokes at the desired temporal positions
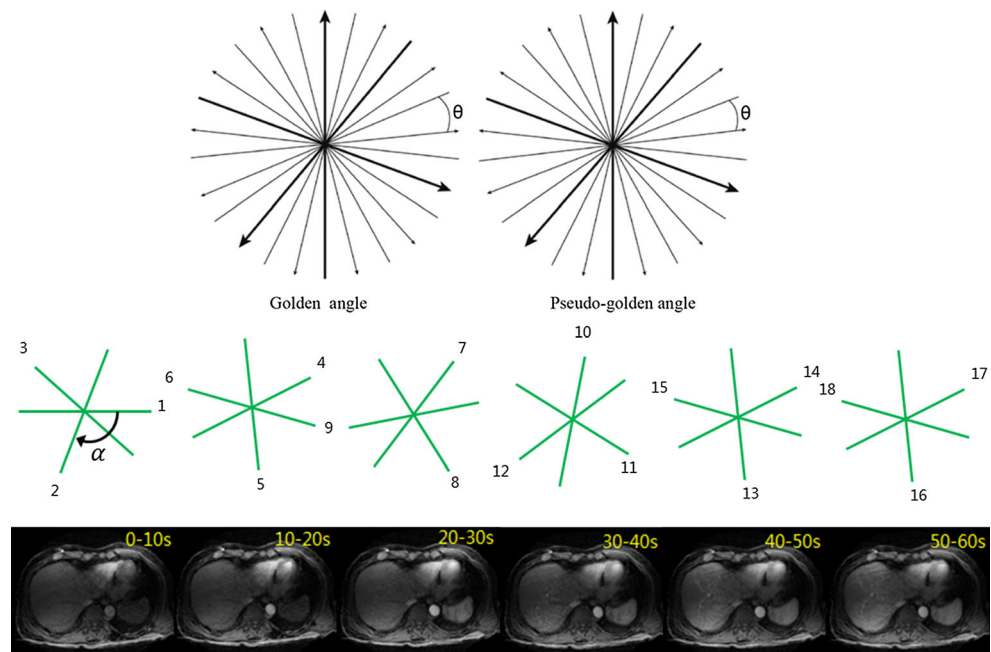
reconstruct one phase (i.e., temporal window = 8.8 s). When 379 radial spokes were acquired, $\lfloor 379/55 \rfloor = 6$ phases were produced. First, a 1D inverse Fourier transform was performed along kz to obtain (kr, kθ, z, coil, phase, echo). For a given z and echo, compressed sensing parallel imaging reconstruction was performed, where the number of iterations was 40. The regularization parameter values of 0.01, 0.1, and 1 were tested to compare the image quality with regard to spatial blurriness and the degree of streak artifact, and the value of 0.1 was chosen as it produced the most adequate image quality. The temporal total variation regularization parameter was 0.1. Spatial regularization was not performed. After image reconstruction was performed in all slices and echoes, the first echo 3D image data (I_{TE1}) and the second echo 3D image data (I_{TE2}) were separately obtained. I_{TE1} and I_{TE2} were used as the input for a water-fat separation algorithm. An in-house water-fat separation method was implemented based on Eggers et al [33].

Image analysis

Two radiologists (J.H.M. and Y.K.K. with 11 and 18 years of experience interpreting liver MRIs, respectively) independently reviewed MRIs in an anonymized and randomized manner, and a consensus was reached afterwards. To minimize any learning bias, there was a 4-week interval between each blinded interpretations.

Image quality analysis

Reviewers assessed image quality of the AP and PVP with regard to respiratory motion artifact or streak artifact, anatomic sharpness of the upper abdominal organ margin (liver, gallbladder, and pancreas), conspicuity of intrahepatic vessels (hepatic artery, portal vein, and hepatic vein), and conspicuity of the hepatic tumor. For the degree of ghosting artifact, we used the following scale: 5, no artifact; 4, minimal artifact with no effect on diagnostic quality; 3, moderate artifact with some effect but no severe effect on diagnostic quality; 2, severe artifact but image was still interpretable; and 1, extensive artifacts resulting in nondiagnostic images [14]. For others, we also used a 5-point scale system in which 1 = unacceptable, 2 = poor, 3 = fair, 4 = good, and 5 = excellent (the detailed definition of scoring system in Supplementary Table E1). Given the similar image quality of the six successively acquired images using PGRA, the third (AP) and sixth (PVP) images were selected for assessment of image quality.

After reviewing individual images, each reader independently reviewed AP and PVP images side-by-side for each patient for pairwise comparison, in which EOB-MRI was the control image, followed by joint evaluation until a consensus was reached. The readers assessed the image sets by considering aforementioned five subjective categories. A semi-quantitative 5-point scale was used (1 = inferior [impairing diagnosis], 2 = slightly inferior [no influence on diagnosis], 3 = equal, 4 = slightly superior [no influence on diagnosis], and 5 = superior [easing diagnosis]) [34].

Diagnostic performance analysis

Reviewers were also asked to record the signal intensity of the hepatic lesion in the AP image, PVP image (two PVP images in PGRA), and 3 min delayed image and categorize the

Table 1 Clinicopathologic characteristics of 15 patients with 18 HCCs

Variables	
Patients	$N = 15$
Age (year)	57.9 (41–69)
Sex	
Male/female	14:1
Etiology	
Hepatitis B	14 (93.3)
Others	1 (6.7)
Liver cirrhosis	11 (73.3)
Child–Pugh A	15 (100.0)
AFP level (ng/mL)	8.7 (1.3–300)
Operation method	
Wedge resection	3 (20.0)
Segmectectomy	3 (20.0)
Sectionectomy	4 (26.7)
Lobectomy	5 (33.3)
No. of HCCs	
One	12 (80.0)
Two	3 (20.0)
Time interval between two MRIs (days)	15 (10–22)
HCC pathological characteristics	$N = 18$
Size (mm)[a]	21.3 (11–34)
Size subgroup	
10–19 mm	7 (38.9)
≥ 20 mm	11 (61.1)
Grade	
I	2 (11.1)
II	13 (72.2)
III	3 (16.7)
Capsule formation	16 (88.9)
Septum formation	16 (88.9)
Fat	1 (5.6)
Necrosis	2 (11.1)
Hemorrhage	3 (16.7)

Except where indicated, numbers in parentheses are percentages

AFP alpha-fetoprotein, *MRI* magnetic resonance imaging, *HCC* hepatocellular carcinoma

[a] Data are presented as median (range)

Table 2 Results of subjective image analysis using a 5-point evaluation scale system for each MR imaging

	Artifact		Organ sharpness		Vessel conspicuity		Lesion conspicuity	
	AP	PVP	AP	PVP	AP	PVP	AP	PVP
EOB-MRI	4.33 ± 0.98	4.73 ± 0.46	4.33 ± 1.05	4.73 ± 0.46	4.40 ± 1.06	4.87 ± 0.35	4.17 ± 1.43	4.39 ± 1.09
ECA-MRI	4.00 ± 0.00	4.00 ± 0.00	4.13 ± 0.35	4.20 ± 0.41	4.60 ± 0.51	4.80 ± 0.41	4.61 ± 0.50	4.61 ± 0.61
p value	0.307	0.001	0.617	0.008	0.500	1.000	0.188	0.375

Data represents mean values ± 1 SD

EOB-MRI gadoxetic acid-enhanced MRI, *ECA-MRI* extracellular contrast-enhanced MRI using pseudo-golden-angle radial acquisition scheme, *AP* arterial phase, *PVP* portal venous phase

hepatic tumor based on the Liver Imaging Reporting and Data System (LI-RADS 2017 version) [35].

Statistical analysis

Statistical analysis was executed using R version 3.4.3 (The R Foundation for Statistical Computing). All comparisons for subjective image ratings for each image and pairwise comparisons were performed using the Wilcoxon test. For pairwise comparisons, we tested a null hypothesis that the two MRIs equal. The kappa statistic for two observers was calculated to assess the inter-observer agreement regarding pairwise comparison. The *p* value < 0.05 was considered significant.

## Results

Clinicopathologic characteristics

Clinicopathologic characteristics of 15 patients with 18 HCCs are demonstrated in Table 1. Most of patients had liver cirrhosis (*N* = 10) or chronic hepatitis B (*N* = 4) associated with hepatitis. HCCs ranged from 11 to 34 mm in diameter (mean

21.3 mm); seven (38.9%) were 10–19 mm, and the remaining 11 (61.1%) were ≥ 20 mm in diameter. On pathology, capsule and septum were present in 16 HCCs (88.9%) and absent in two (11 mm and 12 mm in size). According to Edmondson's classification, 13 (72.2%) HCCs corresponded to grade 2, three (16.7%) were grade 3, and the remaining two (11.1%) were grade 1. The characteristics of a total of 24 observations (18 HCCs, two hemangiomas, and four arterioportal shunts) are shown in Supplementary Table E2.

Individual analysis for each MRI

Table 2 and Fig. 2 summarize the results of the consensus review for image quality of the two MRIs. With regard to the severity of ghosting or streak artifacts, a ghosting artifact was scored category 2 or 3 in the AP of the EOB-MRI in three patients (Figs. 2 and 3). In the AP using ECA-MRI, there was no ghosting artifact, but a mild streaky artifact (scored as category 4) was noted in all 15 patients (Figs. 2 and 3). The difference in mean value for artifacts between the two MRIs was not significant for the AP (*p* = 0.307), but it was significant for the PVP image (*p* = 0.001). The mean value for anatomic sharpness of the upper abdominal organ was slightly

Fig. 2 Image quality analysis according to MRI modality
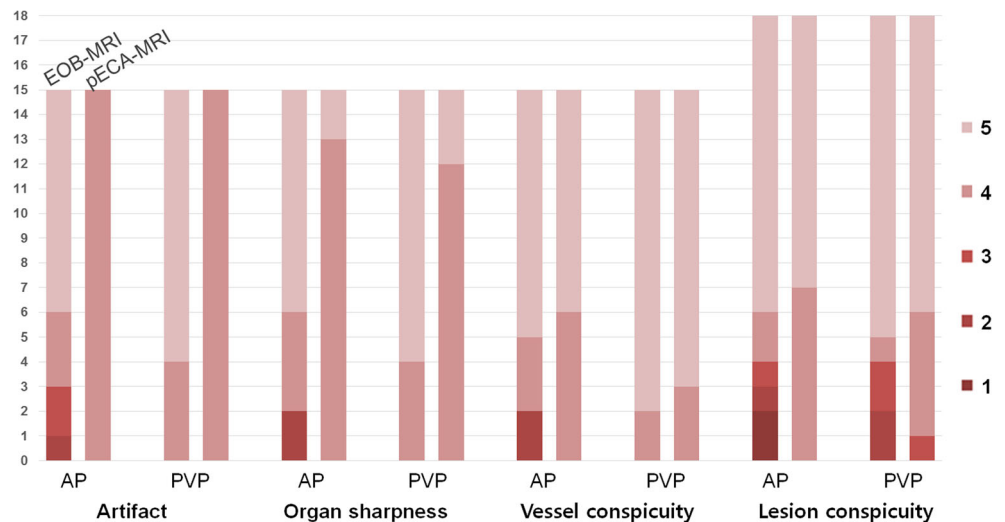
Fig. 3 Comparison between **a** gadoxetic acid-enhanced conventional MR imaging using a Cartesian approach and **b** extracellular contrast-enhanced MR imaging using a pseudo-golden-angle radial acquisition scheme. Ghosting artifacts are observed only in the conventional image (arrows in **a**)
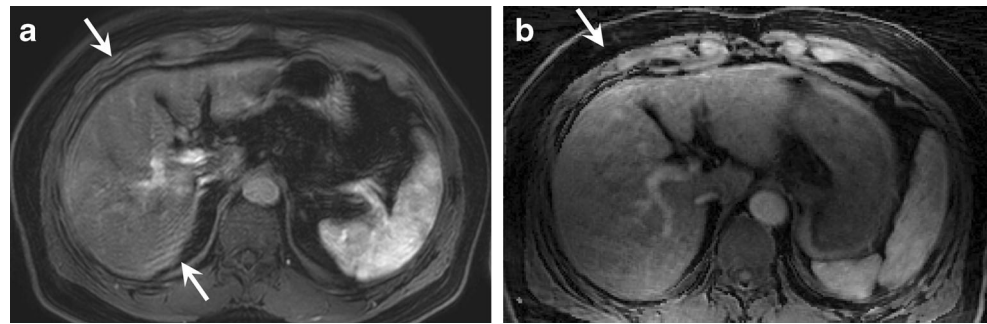
higher in EOB-MRI (mean 4.33 for AP and 4.73 for PVP) than in ECA-MRI (mean 4.13 for AP and 4.20 for PVP), although a statistically significant difference was only achieved for the PVP ($p = 0.008$). With regard to conspicuity of intrahepatic vessels, no significant difference was found either in the AP or PVP (4.87 in EOB-MRI vs. 4.80 in ECA-MRI; $p = 0.500$ or 1.000). Meanwhile, there was no a significant difference in the mean value for conspicuity of the HCCs in the AP and PVP ($p = 0.188$ and $p = 0.375$).

Pairwise comparison between the two MR examinations

In pairwise comparisons of the APs between the two MRIs, there were no significant differences between artifact ($p = 0.076$), organ sharpness ($p = 1.000$), conspicuity of intrahepatic vessels ($p = 0.750$), and conspicuity of the liver mass ($p = 0.125$). In pairwise comparisons of the PVP between the two MRIs, artifact was of EOB-MRI were

Table 3 The result of pairwise comparison between MR sequences

		Artifact	Organ sharpness	Vessel conspicuity	Lesion conspicuity
EOB-MRI-ECA-MRI	AP	2.47 ± 0.92 (range 2–5)	3.07 ± 0.70 (range 2–5)	3.13 ± 0.64 (range 2–5)	3.28 ± 0.58 (range 3–5)
	PVP	2.20 ± 0.41 (range 2–3)	2.87 ± 0.35 (range 2–3)	2.93 ± 0.26 (range 2–3)	3.11 ± 0.47 (range 2–4)
	p value	0.076, 0.0001	1.000, 0.500	0.750, 1.000	0.125, 0.125

Data represents mean values ± standard deviation. Numbers in parentheses represent the range of scoring, respectively. *P* values are AP and PVP, respectively

EOB-MRI gadoxetic acid-enhanced MRI, *ECA-MRI* extracellular contrast agent-enhanced MRI using pseudo-golden-angle radial acquisition scheme, *AP* arterial phase, *PVP* portal venous phase

Table 4 Comparison of MRI modality for major features and LI-RADS categories for HCC diagnosis

	Tumor size	EOB-MRI				ECA-MRI with PGRA			
		APHE	Washout	Capsule	LI-RADS (LR3/LR4/LR5)	APHE	Washout	Capsule	LI-RADS (LR3/LR4/LR5)
Total (N = 18)	…	11 (61.1)	16 (88.9)	6 (33.3)	1/7/10	16 (88.9)	18 (100)	15 (83.3)	0/3/15
Concordances (N = 12)									
N = 10	…	+	+	± (4/6)	LR-5	+	+	+	LR-5
N = 2	…	− (hypo)	+	−	LR-4	− (hypo)	+	−	LR-4
Discordances (N = 6)									
	1.1 cm	− (hypo)	+	−	LR-4	+	+	+	LR-5
	1.2 cm	− (iso)	−	−	LR-3	+	+	−	LR-4
	1.4 cm	− (iso)	+	−	LR-4	+	+	+	LR-5
	2.2 cm	+	−	−	LR-4	+	+	+	LR-5
	2.3 cm	− (iso)	+	+	LR-4	+	+	+	LR-5
	2.8 cm	− (iso)	+	+	LR-4	+	+	+	LR-5

Washout was defined as hypointensity on PVP or DP on ECA-MRI or hypointensity on PVP on EOB-MRI. Numbers in parentheses represent percentages

EOB gadoxetic acid, *ECA* extracellular agent, *PGRA* pseudo-golden-angle radial acquisition scheme, *APHE* arterial phase hyperenhancement, *HCC* hepatocellular carcinoma, *LI-RADS* Liver Imaging Reporting and Data System

significantly lower than that of ECA-MRI ($p = 0.0001$), but other parameters had no significant difference ($p > 0.05$; Table 3). The kappa values of the two observers ranged from 0.628 to 0.700 for the four imaging parameters, indicating good inter-observer agreement.

Diagnostic performance analysis

Ten HCCs showed arterial hyperenhancement, followed by washout on the both MRIs, categorized as LR-5 (Table 4). Two HCCs showed no arterial hyperenhancement and were considered to be hypovascular HCCs, categorized as LR-4 with both MRIs. Six HCCs showed different signal intensities

on the AP or PVP acquired from the two MRI sets. Five of them were assigned as LR-5 with ECA-MRI and LR-4 with EOB-MRI (Table 4). The remaining one was assigned as LR-4 with ECA-MRI and LR-3 with EOB-MRI. Five HCCs showed different signal intensity in the AP image between the two MRIs (Table 4). Of these, a 1.1-cm-sized HCC showed hypointensity on the AP of EOB-MRI due to early acquisition of the AP, but hyperenhancement on AP of ECA-MRI (Fig. 4). In two patients who each had 1.2-cm- and 1.4-cm-sized HCCs, arterial hyperenhancement of the HCCs was clearly seen on ECA-MRI, but not on EOB-MRI, in which the ghosting artifact was assigned as 3 or 2 (Fig. 5). The remaining two HCCs (2.3 and 2.8 cm in size, respectively) did not
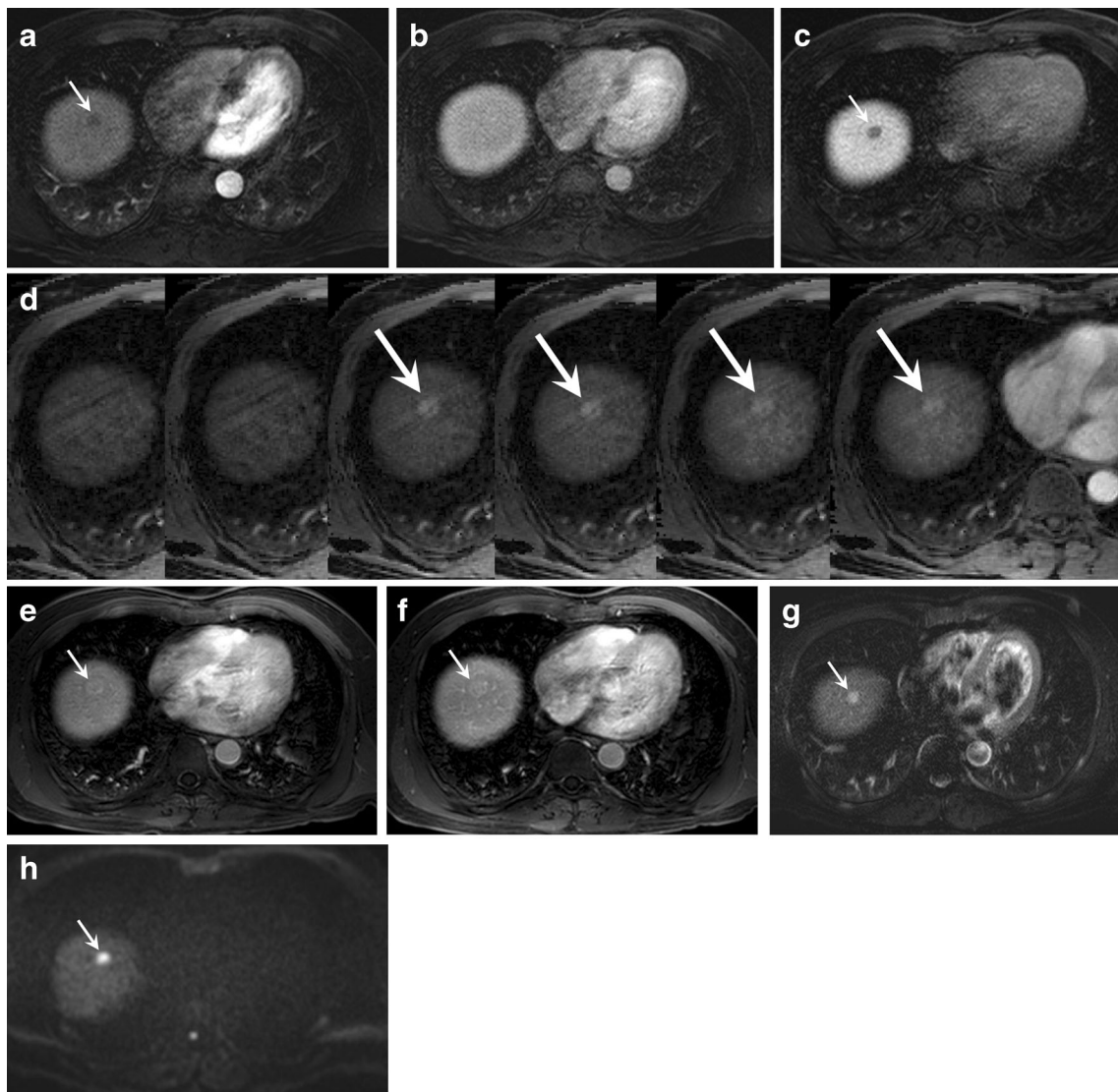
Fig. 4 Edmondson grade II hepatocellular carcinoma in a 62-year-old male. **a** On the axial arterial phase, **b** portal venous phase, and **c** hepatobiliary phase images after administration of gadoxetic acid, an 11-mm-sized liver mass (arrows) is seen as hypointensity. **d** For the six phases successively acquired during the 64 s following administration of extracellular contrast agent, the tumor showed hyperenhancement from the third to sixth phases (arrows). **e** On portal venous phase and **f** delayed phase images, the tumor showed washout with capsule (arrows). Mild streaky artifacts were observed in six phases (**d**), but did not compromise diagnostic image quality. The mass (arrow) shows high signal intensity **g** on the T2-weighted image and **h** on DWI with a b value of 800 s/mm^2
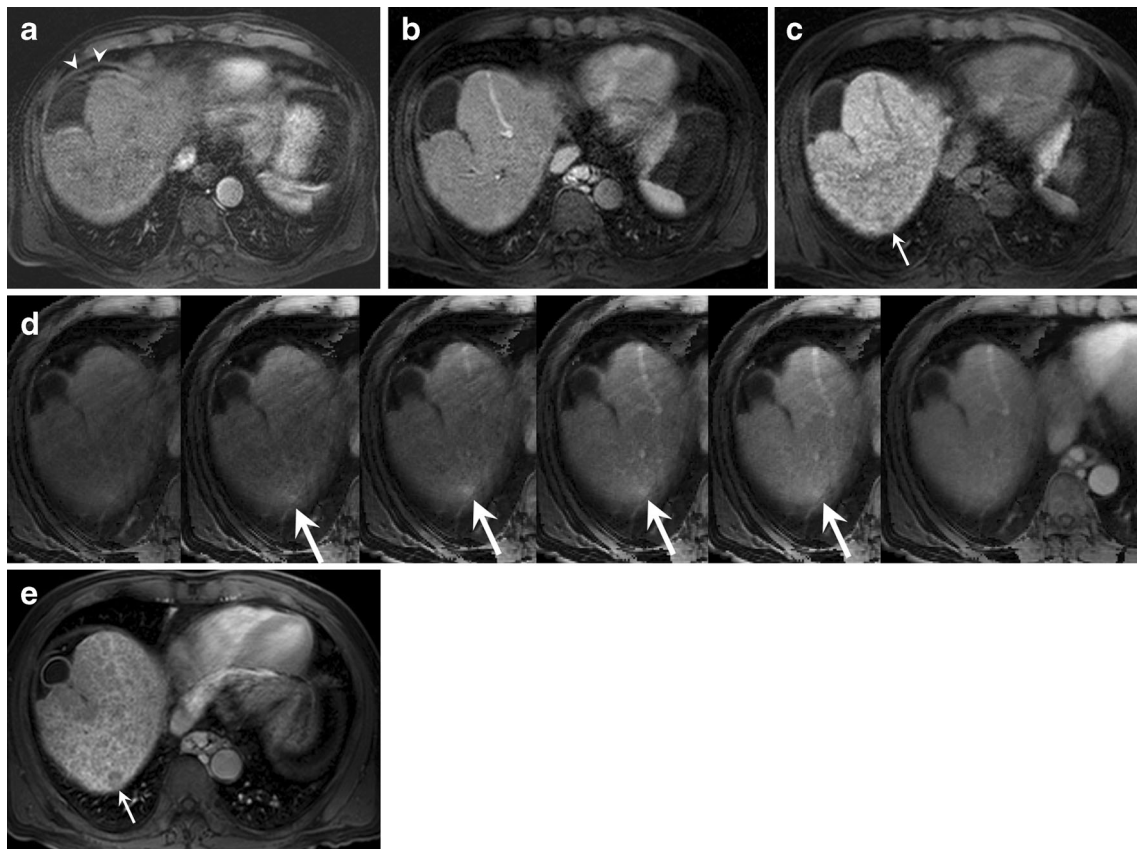
Fig. 5 A 12-mm-sized Edmondson grade II hepatocellular carcinoma in a 65-year-old male. **a** On the axial arterial phase, **b** portal venous phase, and **c** hepatobiliary phase images after administration of gadoxetic acid, arterial hyperenhancement is not clear, and hypointensity on the hepatobiliary phase is suspicious (arrows). A motion artifact (thin arrows) is noticeable in the arterial phase image. For the six phases successively acquired during the 64 s following administration of extracellular contrast agent (**d**), the tumor showed obvious arterial hyperenhancement (arrows), followed by washout on **e** portal venous phase (arrow). Mild streaky artifacts were observed in six phases (**d**)

show arterial hyperenhancement on EOB-MRI due to too early acquisition of the AP, but showed hyperenhancement on the AP of ECA-MRI using PGRA (Fig. 6).

ECA-MRI identified the presence of capsule in 15 HCCs as an enhancing rim encircling the tumor on the PVP and/or the delayed phase. Meanwhile, EOB-MRI demonstrated the enhancing capsule in only six HCCs. In case of a 2.2-cm HCC, ECA-MRI demonstrated arterial hyperenhancement, delayed washout, and a capsule, whereas EOB-MRI failed to show washout and capsule on the PVP.

Discussion

In the current study, we conducted an intra-individual comparison in a crossover manner, addressing the following two questions raised during clinical examination. (1) Is PGRA actually beneficial for capturing the arterial hyperenhancement of HCC compared with conventional dynamic images based on Cartesian sampling schemes? (2) Is PGRA useful for minimizing ghosting artifacts that can be observed in the AP of conventional MRI using a Cartesian approach? In addition, we examined the difference of the HCC enhancement pattern between EBO-MRI and ECA-MRI, which might lead to a difference in tumor categorization based on LI-RADS.

From the technical perspective of the first issue, given the fact that the actual gadolinium concentration of the two contrast agents were different (gadoxetic acid 0.025 mmol/kg vs. ECA 0.1 mmol/kg) [19], it is unlikely that the technical superiority of PGRA over the Cartesian approach accounts for the overall trend that we found. Of note, a previous study described that no significant difference existed in terms of delineation of arterial hyperenhancement of HCC between EOB-MRI and ECA-MRI [36]. Thus, we believe that in addition to the higher concentration of gadolinium of ECA compared with that of gadoxetic acid, the continuous data acquisition scheme in PGRA during the 64 s after contrast administration could have served as a contributing factor. The small dose of gadoxetic acid can cause difficulty in catching the optimal scan time for obtaining late AP after bolus administration of the contrast agent which would be most effective for visualizing HCC. In our study, EOB-MRI did not sufficiently depict the arterial hyperenhancement of five small HCCs, of which ECA-MRI using PGRA clearly depicted. The AP of EOB-
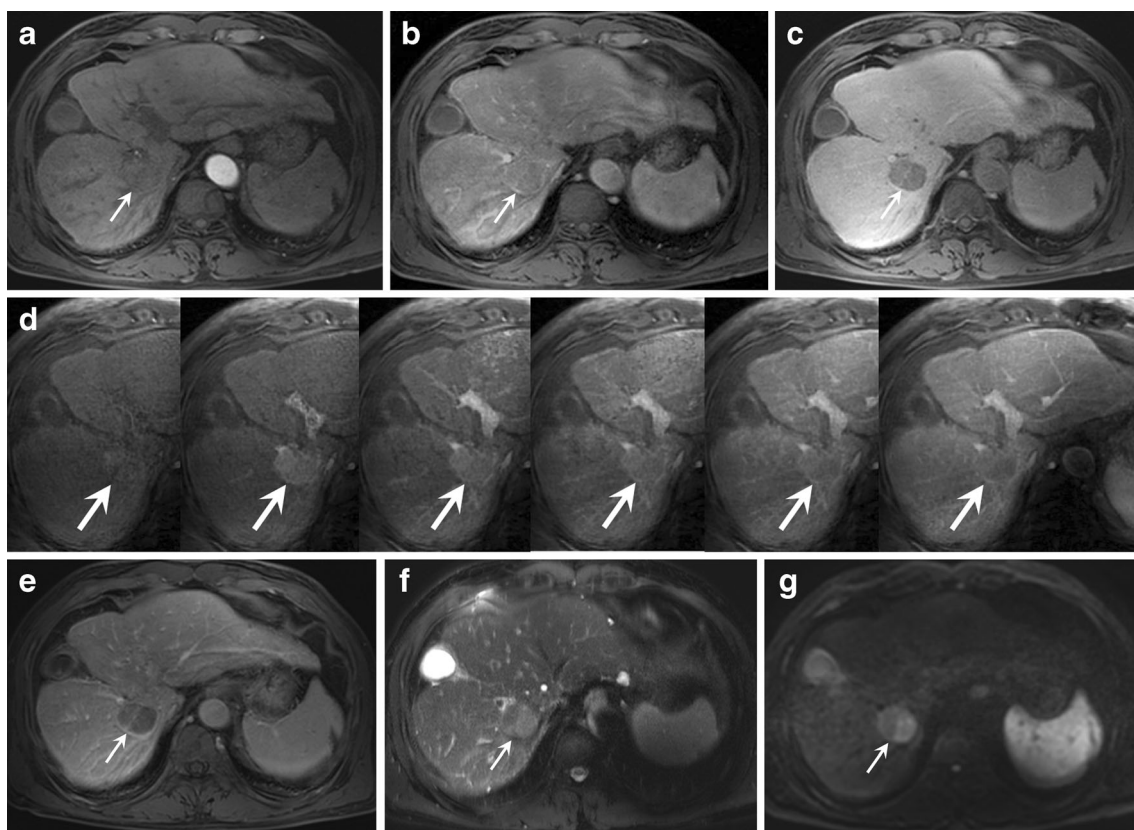
Fig. 6 A 28-mm-sized Edmondson grade II hepatocellular carcinoma in a 62-year-old male. **a** On the axial arterial phase, **b** portal venous phase, and **c** hepatobiliary phase images after administration of gadoxetic acid, arterial hyperenhancement and washout are not clear, and hypointensity on the hepatobiliary phase is seen (arrows). **d** For the six phases successively acquired during the 64 s following administration of extracellular contrast agent, the tumor showed obvious arterial hyperenhancement (arrows), followed by washout on **e** portal venous phase (arrow). Mild streaky artifacts were observed in six phases (**d**). The mass (arrow) shows high signal intensity **f** on the T2-weighted image and **g** on DWI with a *b* value of 800 s/mm^2

MRI in three of the five patients was acquired too early that enhancement in the central portal vein was not observed [37]. In addition, in three patients, a ghosting artifact was observed on the AP of EOB-MRI, which might interfere with the detection of HCC. Meanwhile, no patient showed a ghosting artifact in ECA-MRI using PGRA. Thus, our observation indicates that a continuous data acquisition scheme using PGRA can be applied to optimally acquire the late AP and therefore effectively reveal the arterial hyperenhancement of HCC.

One concern with the radial acquisition scheme is the streak artifacts, as undersampling in the azimuthal direction maintains the overall image structure and results in streaks instead of the backfolding or discrete ghosting artifacts which is typically observed with Cartesian sampling [23]. We observed streak artifacts in all 15 patients enrolled in our study particularly on the dome portion of the liver, although this did not seem to compromise with the diagnostic capacity (Fig. 3d). In the AP, there were no significant differences between the two MRI sets with regard to image quality. Notably, there are other factors contributing to artifact in radial acquisition but not in Cartesian acquisition. Off-resonance can contribute to blurring artifact. Field inhomogeneity is

relatively large near the patient arms far from the isocenter. It is known that the use of coil element removal, although not performed in this study, is potentially helpful in artifact reduction in an off-line reconstruction. Gradient timing delay can be another factor contributing to image quality degradation. An off-line correction of the gradient timing delay may be helpful in artifact reduction although the calibration for gradient delay correction can be made during pulse sequence development in the axial scan plane, which was the scan orientation in this study.

Given that gadoxetic acid begins to be taken up by hepatocytes approximately 60 s after contrast injection, the washout appearance on EOB-MRI can be optimally assessed only in the PVP prior to the transitional phase or HBP [38, 39]. However, Okamoto et al showed that certain histologic types of HCC, such as those with better differentiation and trabecular architecture, tend to show continuous enhancement even on the PVP [40]. As expected, in our study, two HCCs were isointense on the PVP of the two MRIs, but showed washout with a capsule only on the delayed phase of ECA-MRI. In addition, ECA-MRI revealed an enhancing capsule in 15 HCCs, but EOB-MRI demonstrated a corresponding structure

in only 6 HCCs. Thus, if HCC diagnosis was established based on the imaging criteria of LR-5, the sensitivity of ECA-MRI ($N = 15$, 83.3%) was higher than that of EOB-MRI ($N = 10$, 55.6%). The results of our study implies that ECA-MRI with PGRA can be more effective in the HCC diagnosis when applying stringent criteria, at the cost of minimal streaky artifact which did not interfere with the detection of tumor hypervascularity. In particular, we believe that free-breathing PGRA scheme is desirable in patients who cannot adequately hold their breath.

There are several limitations in our study that deserve mention. First, the unbalanced comparison between EOB-MRI and ECA-MRI might have partly acted as a bias in determining the pure technical benefit of the PGRA scheme with regard to delineation of arterial hyperenhancement of HCCs and reduce the ghosting artifact. Thus, our results partly support the technical superiority of PGRA over the conventional approach. Second, a limited number of patients were enrolled in the present study. Third, a selection bias may exist with regard to the initial imaging referrals as we recruited only patients suspected of having HCC who were scheduled to undergo surgical resection.

In conclusion, the free-breathing ECA-enhanced multiphasic liver MRI using a PGRA scheme offers higher detectability of arterial hyperenhancement of HCC than conventional EOB-MRI, while offering acceptable image quality for HCC diagnosis.

Compliance with ethical standards

Guarantor The scientific guarantor of this publication is Sun Jin Lee in Department of Radiology and Center for Imaging Science, Samsung Medical Center, Sungkyunkwan University School of Medicine, Seoul, Republic of Korea.

Conflict of interest The authors of this manuscript declare no relationships with any companies, whose products or services may be related to the subject matter of the article.

Statistics and biometry Soohyun Ahn (author) who is working as an associate professor at the Department of Mathematics of Ajou University is responsible for the statistical analysis of this study.

Informed consent Written informed consent was obtained from each patient before enrollment in the study.

Ethical approval This prospective study was approved by our institutional review board and followed the Declaration of Helsinki and subsequent amendments.

Methodology
• Prospective
• Case-control study
• Performed at one institution

References

1. Lee YJ, Lee JM, Lee JS et al (2015) Hepatocellular carcinoma: diagnostic performance of multidetector CT and MR imaging—a systematic review and meta-analysis. Radiology 275:97–109
2. Khalili K, Kim TK, Jang HJ et al (2011) Optimization of imaging diagnosis of 1-2 cm hepatocellular carcinoma: an analysis of diagnostic performance and resource utilization. J Hepatol 54:723–728
3. Marin D, Di Martino M, Guerrisi A et al (2009) Hepatocellular carcinoma in patients with cirrhosis: qualitative comparison of gadobenate dimeglumine-enhanced MR imaging and multiphasic 64-section CT. Radiology 251:85–95
4. Bruix J, Sherman M (2011) Management of hepatocellular carcinoma: an update. Hepatology 53:1020–1022
5. Fujita N, Nishie A, Kubo Y et al (2015) Hepatocellular carcinoma: clinical significance of signal heterogeneity in the hepatobiliary phase of gadoxetic acid-enhanced MR imaging. Eur Radiol 25:211–220
6. Onishi H, Kim T, Imai Y et al (2012) Hypervascular hepatocellular carcinomas: detection with gadoxetate disodium-enhanced MR imaging and multiphasic multidetector CT. Eur Radiol 22:845–854
7. Akai H, Yasaka K, Nojima M et al (2018) Gadoxetate disodium-induced tachypnoea and the effect of dilution method: a proof-of-concept study in mice. Eur Radiol 28:692–697
8. Pietryga JA, Burke LM, Marin D, Jaffe TA, Bashir MR (2014) Respiratory motion artifact affecting hepatic arterial phase imaging with gadoxetate disodium: examination recovery with a multiple arterial phase acquisition. Radiology 271:426–434
9. Yoo JL, Lee CH, Park YS et al (2016) The short breath-hold technique, controlled aliasing in parallel imaging results in higher acceleration, can be the first step to overcoming a degraded hepatic arterial phase in liver magnetic resonance imaging: a prospective randomized control study. Invest Radiol 51:440–446
10. Park YS, Lee CH, Yoo JL et al (2016) Hepatic arterial phase in gadoxetic acid-enhanced liver magnetic resonance imaging: analysis of respiratory patterns and their effect on image quality. Invest Radiol 51:127–133
11. Park YS, Lee CH, Kim IS et al (2014) Usefulness of controlled aliasing in parallel imaging results in higher acceleration in gadoxetic acid-enhanced liver magnetic resonance imaging to clarify the hepatic arterial phase. Invest Radiol 49:183–188
12. Kim SM, Heo SH, Kim JW et al (2014) Hepatic arterial phase on gadoxetic acid-enhanced liver MR imaging: a randomized comparison of 0.5 mL/s and 1 mL/s injection rates. Korean J Radiol 15:605–612
13. Tamada T, Ito K, Yoshida K et al (2011) Comparison of three different injection methods for arterial phase of Gd-EOB-DTPA enhanced MR imaging of the liver. Eur J Radiol 80:e284–e288
14. Kim YK, Lin WC, Sung K et al (2017) Reducing artifacts during arterial phase of gadoxetate disodium-enhanced MR imaging: dilution method versus reduced injection rate. Radiology 283:429–437
15. Song JS, Choi EJ, Park EH, Lee JH (2018) Comparison of transient severe motion in gadoxetate disodium and gadopentetate dimeglumine-enhanced MRI: effect of modified breath-holding method. Eur Radiol 28:1132–1139
16. Gutzeit A, Matoori S, Froehlich JM et al (2016) Reduction in respiratory motion artefacts on gadoxetate-enhanced MRI after training technicians to apply a simple and more patient-adapted breathing command. Eur Radiol 26:2714–2722
17. Weiss J, Taron J, Othman AE et al (2017) Feasibility of self-gated isotropic radial late-phase MR imaging of the liver. Eur Radiol 27:985–994
18. Koda M, Matsunaga Y, Ueki M et al (2004) Qualitative assessment of tumor vascularity in hepatocellular carcinoma by contrast-enhanced coded ultrasound: comparison with arterial phase of

dynamic CT and conventional color/power Doppler ultrasound. Eur Radiol 14:1100–1108

19. Rohrer M, Bauer H, Mintorovitch J, Requardt M, Weinmann HJ (2005) Comparison of magnetic properties of MRI contrast media solutions at different magnetic field strengths. Invest Radiol 40: 715–724

20. Min JH, Kim YK, Kang TW et al (2018) Artifacts during the arterial phase of gadoxetate disodium-enhanced MRI: multiple arterial phases using view-sharing from two different vendors versus single arterial phase imaging. Eur Radiol 28:3335–3346

21. Lustig M, Donoho D, Pauly JM (2007) Sparse MRI: the application of compressed sensing for rapid MR imaging. Magn Reson Med 58:1182–1195

22. Chandarana H, Feng L, Block TK et al (2013) Free-breathing contrast-enhanced multiphase MRI of the liver using a combination of compressed sensing, parallel imaging, and golden-angle radial sampling. Invest Radiol 48:10–16

23. Chandarana H, Block TK, Rosenkrantz AB et al (2011) Free-breathing radial 3D fat-suppressed T1-weighted gradient echo sequence: a viable alternative for contrast-enhanced liver imaging in patients unable to suspend respiration. Invest Radiol 46:648–653

24. Chandarana H, Feng L, Ream J et al (2015) Respiratory motion-resolved compressed sensing reconstruction of free-breathing radial acquisition for dynamic liver magnetic resonance imaging. Invest Radiol 50:749–756

25. Yoon JH, Lee JM, Yu MH et al (2018) Evaluation of transient motion during gadoxetic acid-enhanced multiphasic liver magnetic resonance imaging using free-breathing golden-angle radial sparse parallel magnetic resonance imaging. Invest Radiol 53:52–61

26. Feng L, Grimm R, Block KT et al (2014) Golden-angle radial sparse parallel MRI: combination of compressed sensing, parallel imaging, and golden-angle radial sampling for fast and flexible dynamic volumetric MRI. Magn Reson Med 72:707–717

27. Winkelmann S, Schaeffter T, Koehler T, Eggers H, Doessel O (2007) An optimal radial profile order based on the golden ratio for time-resolved MRI. IEEE Trans Med Imaging 26:68–76

28. Chan RW, Ramsay EA, Cheung EY, Plewes DB (2012) The influence of radial undersampling schemes on compressed sensing reconstruction in breast MRI. Magn Reson Med 67:363–377

29. Usman M, Atkinson D, Odille F et al (2013) Motion corrected compressed sensing for free-breathing dynamic cardiac MRI. Magn Reson Med 70:504–516

30. Hedderich DM, Weiss K, Spiro JE et al (2018) Clinical evaluation of free-breathing contrast-enhanced T1w MRI of the liver using pseudo golden angle radial k-space sampling. Rofo 190:601–609

31. Chandarana H, Block TK, Ream J et al (2015) Estimating liver perfusion from free-breathing continuously acquired dynamic gadolinium-ethoxybenzyl-diethylenetriamine pentaacetic acid-enhanced acquisition with compressed sensing reconstruction. Invest Radiol 50:88–94

32. Uecker M, Ong F, Tamir J et al (2015) Berkeley advanced reconstruction toolbox. In: Proceedings of the 23rd Annual Meeting of ISMRM, Toronto, p 2486

33. Eggers H, Brendel B, Duijndam A, Herigault G (2011) Dual-echo Dixon imaging with flexible choice of echo times. Magn Reson Med 65:96–107

34. Deák Z, Grimm JM, Treitl M et al (2013) Filtered back projection, adaptive statistical iterative reconstruction, and a model-based iterative reconstruction in abdominal CT: an experimental clinical study. Radiology 266:197–206

35. Elsayes KM, Hooker JC, Agrons MM et al (2017) 2017 version of LI-RADS for CT and MR imaging: an update. Radiographics 37: 1994–2017

36. Park G, Kim YK, Kim CS, Yu HC, Hwang SB (2010) Diagnostic efficacy of gadoxetic acid-enhanced MRI in the detection of hepatocellular carcinomas: comparison with gadopentetate dimeglumine. Br J Radiol 83:1010–1016

37. Mori K, Yoshioka H, Takahashi N et al (2005) Triple arterial phase dynamic MRI with sensitivity encoding for hypervascular hepatocellular carcinoma: comparison of the diagnostic accuracy among the early, middle, late, and whole triple arterial phase imaging. AJR Am J Roentgenol 184:63–69

38. Joo I, Lee JM, Lee DH, Jeon JH, Han JK, Choi BI (2015) Noninvasive diagnosis of hepatocellular carcinoma on gadoxetic acid-enhanced MRI: can hypointensity on the hepatobiliary phase be used as an alternative to washout? Eur Radiol 25:2859–2868

39. Doo KW, Lee CH, Choi JW, Lee J, Kim KA, Park CM (2009) "Pseudo washout" sign in high-flow hepatic hemangioma on gadoxetic acid contrast-enhanced MRI mimicking hypervascular tumor. AJR Am J Roentgenol 193:W490–W496

40. Okamoto D, Yoshimitsu K, Nishie A et al (2012) Enhancement pattern analysis of hypervascular hepatocellular carcinoma on dynamic MR imaging with histopathological correlation: validity of portal phase imaging for predicting tumor grade. Eur J Radiol 81: 1116–1121